Ambient-pressure superconductivity in covalent Au-B frameworks stabilized by electropositive metals

Check for updates

Shuai Han[1], Xiaohua Zhang [ORCID][1], Li Zhu [ORCID][2] ✉, Sheng Wang[1], Shicong Ding[1], Eva Zurek [ORCID][3] ✉ & Guochun Yang [ORCID][1,4] ✉

Extended covalent compounds that contain gold are virtually unknown because Au prefers metallic or molecular coordination. Using crystal structure search combined with first-principles calculations at high pressure, we have identified a family of ternary compounds, M_2AuB_6 (M = Na, K, Mg, Ca, and Sr), featuring Au-B covalent frameworks that satisfy a simple "push-pull" design rule: strongly electropositive cations donate charge that anchors Au in electron-deficient B_6 octahedra, thereby stabilizing Au–B σ bonds through Au dsp^2 hybridization. The low enthalpy phases, Na_2AuB_6 and K_2AuB_6, exhibit superconductivity, with Au-$6p_x$/$6p_y$ and B-2p states contributing to Cooper pair formation, facilitated by low- and medium-frequency phonons arising from Au−B bond stretching. These pressure-induced structures and bonding configurations can be quenched to ambient pressure, demonstrating an effective approach to bypassing traditional electronegativity constraints. We propose M_2AuB_6 compounds as realistic and chemically unique platforms for exploring gold-based superconductivity and for testing electron-donor-guided materials discovery.

Chemical bonding is intertwined with the stability, properties, and behavior of matter, serving as the essential link between atomic interactions and macroscopic functionalities[1–5]. Emerging bonding paradigms—such as multi-center bonds[6,7], high-pressure-stabilized bonds[8–10], and bonds influenced by relativistic effects[11,12]—challenge traditional theories and offer valuable insights into unconventional interactions. These mechanisms have led to the discovery of materials with extraordinary properties, such as high-temperature superconductivity[13–15] and ultra-hardness[16–18]. Yet, one conspicuous gap remains: extended covalent frameworks that incorporate gold.

Gold, known for its strong relativistic effects, exhibits distinctive physical and chemical properties in both elemental and compound forms[19–23]. Its relativistic effects induce contraction of the 6 *s* orbital alongside slight radial expansion and energetic stabilization of the 5 *d* orbitals, endowing gold with unique bonding configurations[11,24], rich oxidation states (ranging from −3 to +6)[25–27], and unusual aurophilic interactions[28,29]. These properties place gold at the forefront of studies exploring unconventional bonding and electronic properties, making it a key element in materials science[30–33].

Boron, on the other hand, stands out as an electron-deficient element with an unparalleled ability to form diverse multi-center bonds, fundamentally broadening our understanding of chemical bonding[34–38]. Boron-

based compounds exhibit exceptional properties, including high chemical stability, exceptional mechanical strength[39–41], large nonlinear optical response[42–44], and high conductivity[45–47], with some even displaying superconductivity[48–50]. For instance, MgB_2, a prototypical boride superconductor with the highest transition temperature ($T_c = 39$ K) among ambient-pressure conventional superconductors, features two superconducting gaps—one associated with strong-coupling σ bands and the other with weaker π bands[50,51]. These unique features arise not solely from boron itself but from its interplay with the crystal structure, electronic configuration, and interatomic interactions in the compounds. Nonetheless, the presence of boron contributes significantly to enabling such functionalities through its versatile bonding characteristics and electronic richness.

In molecular chemistry these features enable the formation of isolated Au–B covalent bonds stabilized by bulky ligands or cluster confinement[52–54]. Translating such bonds into an infinite solid, however, has remained elusive. Although an early report described an AlB_2-type AuB_2 phase[55], subsequent analyses indicate that the Au–B interactions in this structure are predominantly ionic rather than covalent[56,57]. The comparable electronegativities[58,59] of Au and B (as exemplified by the Au-H system[60]), hinder the formation of strongly polar Au–B covalency, and the enthalpic contribution to the free energy disfavors

[1]State Key Laboratory of Metastable Materials Science & Technology and Hebei Key Laboratory of Microstructural Material Physics, School of Science, Yanshan University, Qinhuangdao, China. [2]Department of Physics, Rutgers University, Newark, NJ, USA. [3]Department of Chemistry, State University of New York at Buffalo, Buffalo, NY, USA. [4]Centre for Advanced Optoelectronic Functional Materials Research and Key Laboratory for UV Light-Emitting Materials and Technology of Ministry of Education, Northeast Normal University, Changchun, China. ✉e-mail: li.zhu@rutgers.edu; ezurek@buffalo.edu; yanggc468@nenu.edu.cn

binary Au-B compound formation. Thus far, no crystallographically authenticated bulk phase exhibiting an extended Au–B covalent framework has yet been established, leaving both the geometry and electronic consequences of Au–B covalency in extended solids unexplored.

To overcome this intrinsic thermodynamic barrier, we propose a strategy inspired by "push–pull" principle[61], previously demonstrated to effectively redistribute charge and stabilize unconventional materials in multicomponent systems[62–64]. In this framework, strongly electropositive calcium element is introduced to modulate the electron distribution within the Au-B system. Calcium atoms act as electron donors, effectively pushing electrons toward the electron-deficient boron sublattice, while simultaneously pulling electron density into the Au-centered orbitals. This dual modulation results in the accumulation of charge density on Au atoms, thereby promoting orbital interactions and enhancing the covalent character of the Au–B bonds. When further combined with pressure tuning, this approach enables precise control over energy-level alignment and bonding configurations, providing a powerful means to stabilize Au–B interactions in boron-rich compounds.

Using this strategy and first-principles calculations, we predict a metastable metallic phase, Ca_2AuB_6, at 50 GPa. This compound features four-coordinate Au−B bonds stabilized by dsp^2 hybridization of Au. Remarkably, this bonding configuration remains stable in related compounds, such as Na_2AuB_6 and K_2AuB_6, which exhibit metallized Au−B σ-bonds and are predicted to be superconductors at ambient pressure. Our findings not only fill the gap in Au-B chemistry, but also provide transformative insights into the role of Au−B bonds in stabilizing structures and driving superconductivity.

Results and discussion
Structure and stability

Pressure is widely recognized as a powerful tool for stabilizing distinct structures with unique bonding behaviors and intriguing properties[65–70]. Based on extensive structure searches, including the AuB_2 phase, our constructed convex hull for the Au-B system reveals that even at pressures up to 300 GPa, no stable binary Au-B compounds emerge due to their large positive formation enthalpies (Supplementary Fig. S1). This indicates that pressure alone cannot compensate for the electronegativity difference between Au and B to stabilize binary Au-B compounds. Interestingly, upon incorporating Ca into this system, a metastable phase, Ca_2AuB_6, was identified, lying only 68 meV/atom above the convex hull relative to its most stable decomposition products in the Ca-Au-B system at 50 GPa (Fig. 1a). This value falls within the range of many synthesized metastable materials[71–74]. Phonon dispersion calculations from 0 to 50 GPa revealed no imaginary frequencies across the Brillouin zone (Fig. 1b and Supplementary Fig. S2), confirming its dynamical stability and the potential for quenching to ambient pressure. To be noted, the Ca-Au-B ternary phase diagram also includes several other metastable phases (Supplementary Fig. S3) featuring discrete Au and B structural motifs, along with the stable Ca-Au compounds (e.g., $CaAu_3$, Ca_2Au_3, $CaAu$, Ca_3Au_2, Ca_2Au and Ca_3Au, Supplementary Fig. S4), which will be published in future work. Structural predictions and stability analyses used the PBE functional, validated by known pressure-induced phase transitions of Ca, Au, and B (Supplementary Fig. S5).

Ca_2AuB_6 crystallizes in a tetragonal structure with $P4/mmm$ symmetry, featuring a three-dimensional Au-B framework (Fig. 1d). At ambient pressure, the B atoms occupy two inequivalent sites: B1 at 4j (0.8216, 0.1784, 0.0000) and B2 at 2g (0.0000, 0.0000, 0.7064). These atoms form B_6 octahedra, with B1 atoms positioned within the basal plane and B2 atoms located at the vertices. The Au atoms coordinate with B1 atoms from four octahedra in the ab-plane, forming a square-planar AuB_4 configuration, while the B2 atoms link the octahedra along the c-axis, resulting in a robustly interwoven Au-B skeleton. The B−B bond lengths (1.73–1.80 Å) are comparable to those in α-B_{12} (1.77 Å)[75]. The Au−B bond length is 2.29 Å, slightly exceeding that in the gold boride complex (~2.19 Å)[52]. The Ca atoms are situated in the channels formed by the Au-B skeleton along the c-axis, forming Ca−B and Ca−Au bond of 2.66–2.78 Å and 3.28 Å, respectively. It
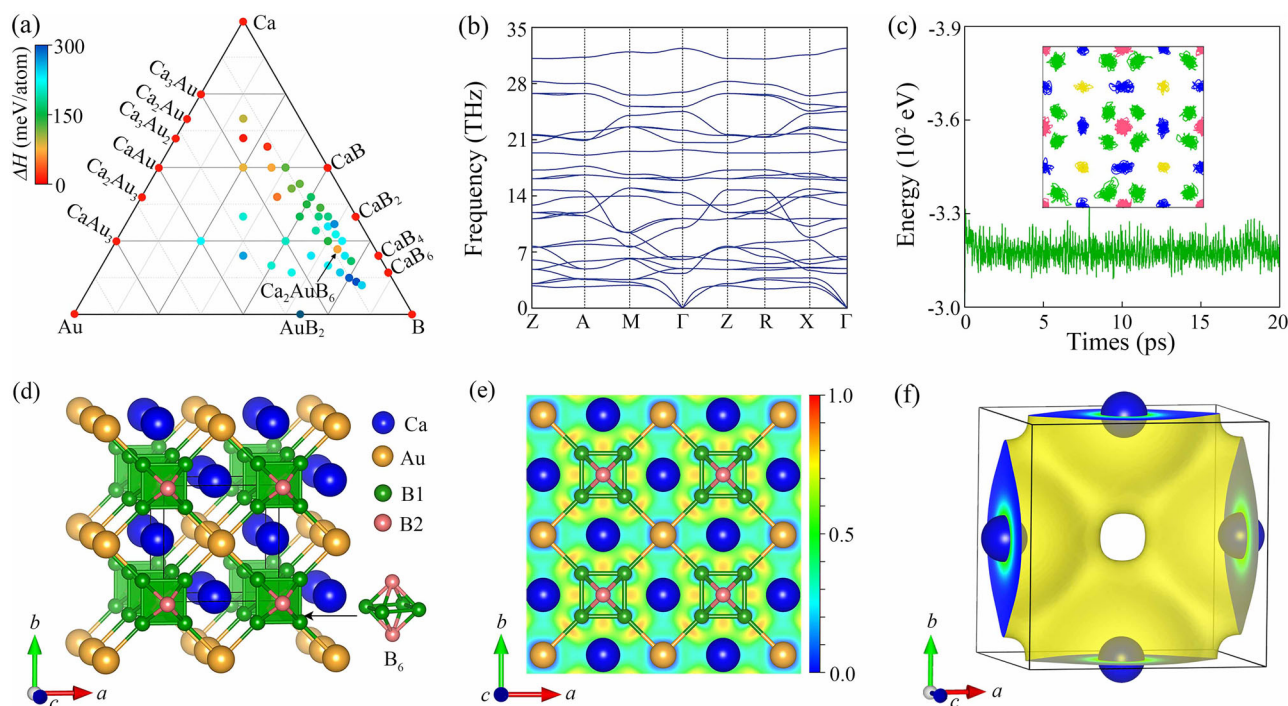

Fig. 1 | Stability, structure, and chemical bonding of Ca_2AuB_6. a Convex hull of predicted Ca-Au-B compounds relative to stable elemental solids and binary compounds at 50 GPa. Fm-$3m$ Au, Pm-$3m$ Ca, and γ-B_{28} were selected as reference elemental structure. The colored circles represent phases that may be thermodynamically stable, metastable or unstable, and the color bar denotes the magnitude of the relative formation enthalpies (ΔH) of the compounds. The AlB_2-type AuB_2[55] with a positive formation enthalpy is also plotted. **b** Phonon dispersion curve of Ca_2AuB_6 at ambient pressure. **c** Free energy as a function of MD time at the temperature of 2800 K for Ca_2AuB_6 at ambient pressure, and the inset illustrates the trajectories of the atoms within Ca_2AuB_6 within the 2 × 2 × 2 supercell after MD equilibration. **d** Predicted crystal structure of $P4/mmm$ Ca_2AuB_6. The blue and golden spheres represent Ca and Au atoms, while the two inequivalent B atoms are denoted by green (B1) and magenta (B2) spheres, respectively. **e** Calculated ELF of Ca_2AuB_6 in the (001) plane. **f** Calculated charge density of Ca sublattice in Ca_2AuB_6, with an isosurface value of 0.008 e/bohr^3.
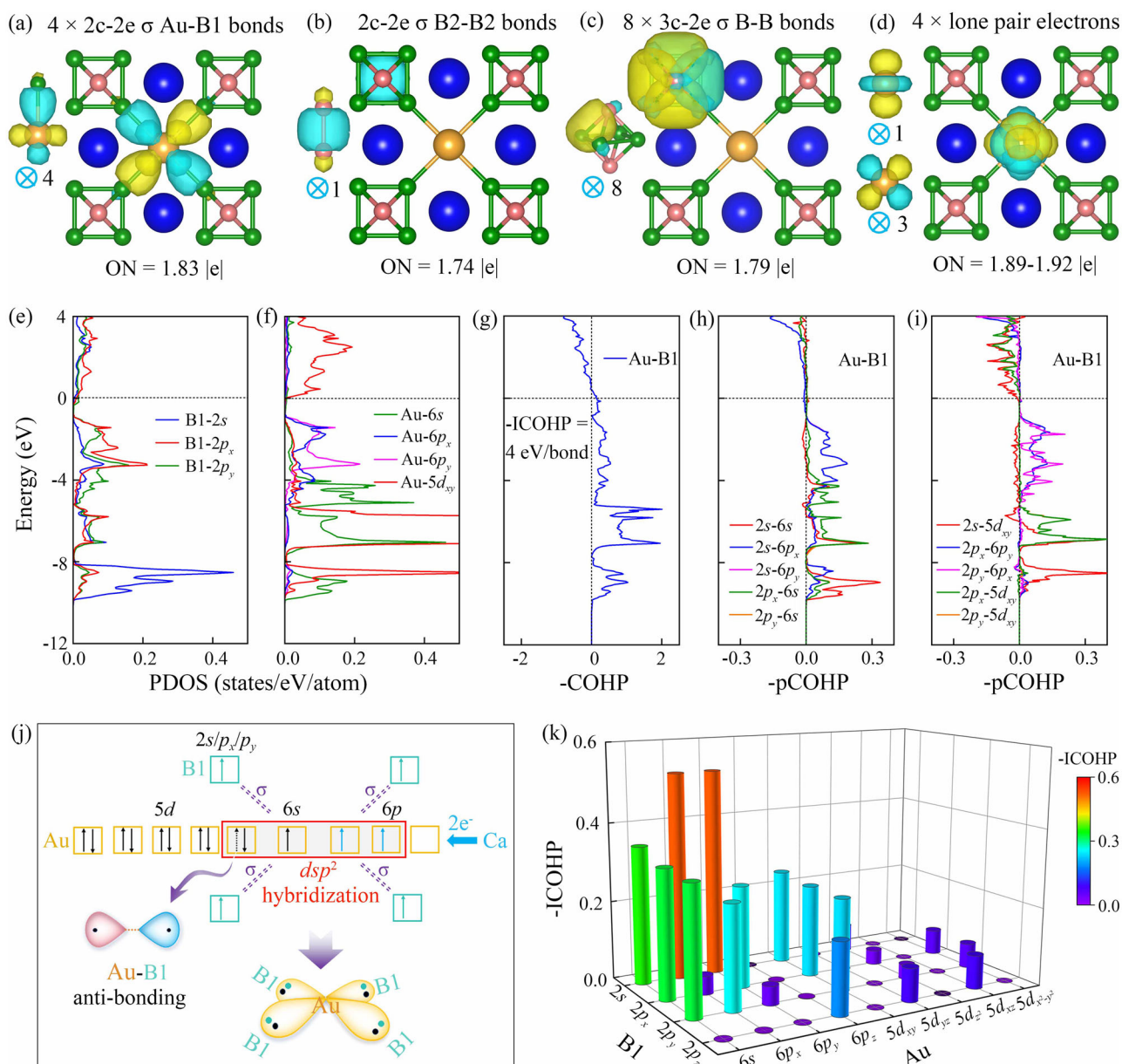
Fig. 2 | Chemical bonding analysis of *P4/mmm* Ca$_2$AuB$_6$ at ambient pressure. **a–d** SSAdNDP analysis along with the occupation number (ON). In total 17 bonds are shown, including four two-center−two-electron (2c−2e) Au−B σ bonds, one 2c−2e B−B σ bond, eight three-center−two-electron (3c−2e) B−B σ bonds, and four lone pairs (LP) on Au. The orbital-resolved PDOS of **e** B1 and **f** Au atoms. Calculated **g** −COHP and **h**, **i** − pCOHP of Au−B1 interaction. Positive and negative values denote bonding and antibonding orbital interactions for COHP, respectively. **j** − ICOHP values between Au and B1 atom pairs. Positive −ICOHP values represent bonding states. **k** The schematic diagram of the formation of Au−B covalent bonds via *dsp²* hybridization in Ca$_2$AuB$_6$, along with the anti-bonding contribution to the Au−B1 bond from the Au 5*d$_{xy}$* states.

is worth noting that *P4/mmm* structures have been previously reported in Au-based ternary systems, including both perovskite-type and structurally simpler compounds[76,77]. Taken together with its robust Au-B skeleton and favorable thermodynamic and dynamical stability, these features suggest that Ca$_2$AuB$_6$ may be experimentally accessible under proper conditions.

Chemical bonding analysis

We subsequently investigate the chemical bonding attributes and stability mechanism of Ca$_2$AuB$_6$ at ambient pressure using Bader charge analysis, electron localization functions (ELF), and solid state adaptive natural density partitioning (SSAdNDP). Significant charge transfer occurs from the Ca atoms to the Au-B framework, resulting in ionic Ca−Au and Ca−B bonds. High ELF values are observed at the center of B−B bonds (Fig. 1e), signifying strong covalent bonding. In contrast, the regions of high ELF values

along the Au−B bonds are polarized towards the B atoms, indicating the presence of polar covalent interactions. The charge density of the Ca sublattice (Fig. 1f) shows significant electron accumulation in the interstitial regions near the original Au-B framework, which stabilizes the Au-B network and resembles the chemical template effect[78]. The SSAdNDP analysis[79] identified several key bonding features: one two-center−two-electron (2c−2e) B−B σ bond, eight 3c−2e B−B σ bonds, four 2c−2e Au−B σ bonds, and four lone pair (LP) electrons of Au (Fig. 2a−d and Supplementary Fig. S6). This Ca$_2$AuB$_6$ structure, featuring a multicenter-bonded Au−B polyanionic anionic network with covalently bonded B$_6$ octahedra and AuB$_4$ units, exhibits substantial charge transfer from the Ca cations and can be classified as a polar intermetallic[80,81]. Temperature-dependent molecular dynamics (MD) simulations demonstrated that Ca$_2$AuB$_6$ maintains its structural integrity up to 2800 K (Fig. 1c and Supplementary S7),
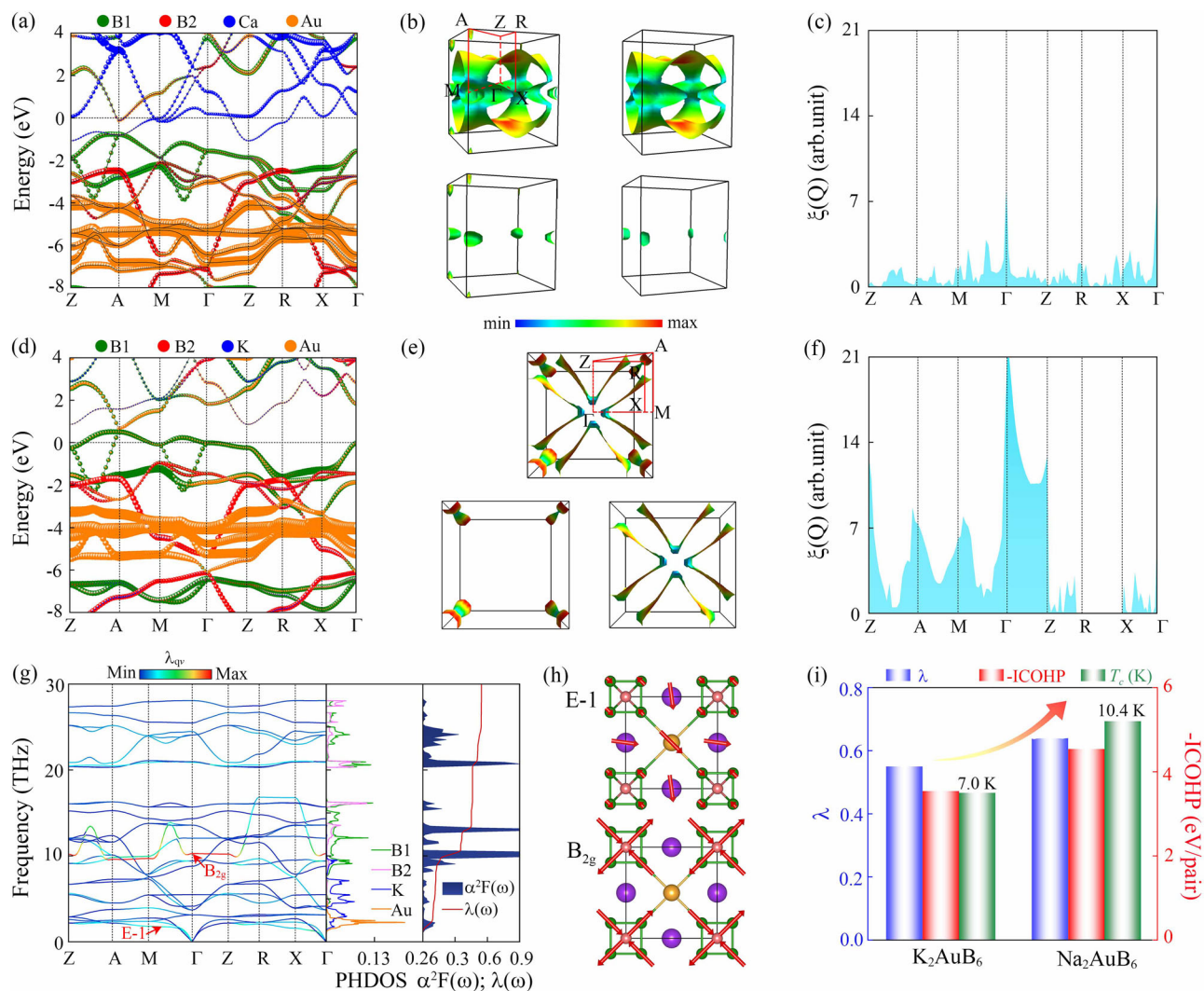
Fig. 3 | Electronic and superconducting properties of M_2AuB_6. Ca_2AuB_6 at ambient pressure: **a** projected electronic band structure, **b** Fermi surfaces with the color drawn proportional to the magnitude of the Fermi velocity, and **c** Fermi surface nesting function, $\xi(Q)$. Na_2AuB_6 at ambient pressure: **d** projected electronic band structure, **e** Fermi surfaces with the color drawn proportional to the magnitude of the Fermi velocity, **f** Fermi surface nesting function, $\xi(Q)$, and **g** phonon dispersions weighted by the magnitude of the electron−phonon coupling EPC (λ_{qv}), projected phonon density (PHDOS), Eliashberg spectral function, $\alpha^2F(\omega)$, and EPC integral, $\lambda(\omega)$. **h** Phonon vibration modes for E-1 and B_{2g} modes, with the red arrows on the atoms indicating the direction of their vibrations. **i** Calculated T_c, λ, and $-ICOHP$ values of Au−B bond for K_2AuB_6 and Na_2AuB_6 at ambient pressure.

highlighting its thermal robustness. Furthermore, the compound meets the criteria for mechanical stability with a calculated Vickers hardness of 24.5 GPa (Supplementary Table S3), making it a promising candidate for applications requiring high hardness and thermal resilience.

The square-planar AuB_4 configuration provides an excellent framework to investigate the valence electron distribution and hybridization of the Au atom. Projected density of states (PDOS) analysis reveals strong hybridization below the Fermi level between Au and B1 atoms (Fig. 2e, f and Supplementary Fig. S8). This hybridization arises from interactions involving B $2s$−Au $6s/6p_x/6p_y/5d_{xy}$, B $2p_x$−Au $6s/6p_y/5d_{xy}$, and B $2p_y$−Au $6s/6p_x/5d_{xy}$ orbitals (Fig. 2g–i), demonstrating that Au $5d_{xy}$, $6s$, $6p_x$, and $6p_y$ orbitals actively participate in forming Au−B bonds, and Au atom shows a dsp^2 hybridization. In Ca_2AuB_6, electron donation from Ca atoms leads to charge accumulation on Au. Mulliken orbital population analysis indicates that the additional electrons are primarily distributed in the Au $6s$ and $6p$ orbitals (Supplementary Table S4). Meanwhile, the Au $5d_{xy}$ orbital participates in a dsp^2 hybridization and also contributes to the formation of an Au−B anti-bonding orbital (Fig. 2j). This hybridization mechanism is further validated by crystal orbital Hamilton population (COHP) analysis (Fig. 2k) performed with the LOBSTER code[82,83]. The integral of the COHP (ICOHP)

value, reaching up to −4.00 eV per bond, highlights the significant strength of the Au−B bond[84]. Notably, this dsp^2 hybridization in the anionic Au differs fundamentally from the hybridization observed in cationic Au (Au^{3+}). In the latter, Au loses three valence electrons to achieve a formal +3 oxidation state, creating four vacant dsp^2 hybrid orbitals that accept electrons from ligands to form coordination bonds[24]. Additionally, PDOS and ICOHP analysis of Ca_2AuB_6 at pressures of 25 and 50 GPa reveal its pressure-insensitive hybridization and robust Au−B bonding (Supplementary Fig. S9 and S10).

Electronic and superconducting properties

We also explored the response of the Au-B framework to the nature of the cationic species by substituting the Ca atom with various alkali and alkaline earth metals, resulting in the formation of four dynamically stable M_2AuB_6 (M = Na, K, Mg, and Sr) compounds at ambient pressure (Supplementary Fig. S11, 12). These compounds also exhibit negative formation enthalpies, indicating their potential thermodynamic accessibility from the selected precursors (Supplementary Fig. S13). The covalency within the Au-B framework remained intact across these substitutions (Supplementary Fig. S14 and Table S5). Band structure calculations (Fig. 3a, d, Supplementary

Fig. S15 and S16a) confirmed metallic behavior, with two or three bands crossing the Fermi level (E_F). However, the origin of the metallicity differs significantly between Na_2AuB_6/K_2AuB_6 and Mg_2AuB_6/Ca_2AuB_6/Sr_2AuB_6. For example, despite similar band dispersion in Ca_2AuB_6 and Na_2AuB_6, the E_F of Ca_2AuB_6 is ~2 eV higher than in Na_2AuB_6 (Fig. 3a, d). This shift arises from the combined influence of differences in valence electron count and elemental characteristics, particularly the substantial contribution of Ca 3d orbitals, along with minor contribution from B1-p_x/p_y and Au-5d_{xy} states in Ca_2AuB_6 (Fig. 3a and Supplementary Fig. S17). Additionally, electron pockets are observed near the A and M points in the Brillouin zone of Ca_2AuB_6. Additionally, the calculations performed with fully relativistic pseudopotentials including explicit spin-orbit coupling show negligible impact on the electronic structure near the E_F (Supplementary Fig. S18), indicating that the scalar-relativistic approximation employed here captures the key electronic feature.

In contrast, the metallic behavior of Na_2AuB_6 is primarily driven by contributions from B1-2p_x/p_y and Au-6p_x/6p_y orbitals (Supplementary Fig. S19a and S20), indicating that electrons in the Au−B bond participate in conductivity. The band structure near E_F exhibits distinct features (Fig. 3d), including flat bands along the Γ−Z direction and around the M point, as well as steep bands along the Z−A direction. We also investigate their Fermi surfaces, whose topological structures reflect the electronic behavior at E_F. In Ca_2AuB_6, three Fermi surfaces are associated with three energy bands that intersect E_F. The first Fermi surface exhibits a porous cylindrical character, originating from a hybridized state of Ca-3d_{x2-y2}/d_{xy}/d_{z2}, B1-2p_x/p_y and Au-5d_{z2}/6p_z orbitals (Fig. 3b and Supplementary Fig. S17). The other two consist of twelve discrete curved surfaces oriented towards the vertices or edge centers of the Brillouin zone, with a major contribution of Ca-3d orbitals. For Na_2AuB_6, two energy bands cross E_F, giving rise to two Fermi surfaces with intriguing topology. One consists of four interconnected, two-dimensional torpedo-like shapes, while the other features four-leaf clover (Fig. 3e). These Fermi surfaces primarily arise from the contribution of B1-2s/2p_x/p_y and Au-5d_{xy}/6p_x/6p_y electronic states (Supplementary Fig. S20). Additionally, Na_2AuB_6 has an obvious nesting behavior along the Z−A−M direction (Fig. 3f), which is slightly stronger than that observed in Ca_2AuB_6 (Fig. 3c). Overall, these electronic characters in Na_2AuB_6 are considered favorable indicators for superconductivity[85,86].

The superconducting transition temperatures (T_c) of M_2AuB_6 compounds were estimated using the Allen-Dynes modified McMillan equation[87], with $\mu^* = 0.1$ (Supplementary Table S6). Mg_2AuB_6, Ca_2AuB_6, and Sr_2AuB_6 remain nonsuperconducting due to their low electron-phonon coupling constants ($\lambda = 0.18-0.21$), much smaller than those of Na_2AuB_6 ($\lambda = 0.64$) and K_2AuB_6 ($\lambda = 0.55$). Correspondingly, Na_2AuB_6 and K_2AuB_6 exhibit higher predicted T_c values of 10.4 K and 7.0 K, exceeding those of typical Au-based superconductors such as Pt-doped $AuTe_2$ (4.0 K)[88,89] and $AuAgTe_4$ (3.5 K)[90]. The Fermi-level DOS of Na_2AuB_6 (10.8 states/spin/Ry/unit cell) is slightly higher than that of K_2AuB_6 (10.7 states/spin/Ry/unit cell), correlating with their λ values and primarily originating from B-2p_x/2p_y and Au-6p_x/6p_y states. Phonon analysis reveals that both low- and mid-frequency acoustic modes dominate λ in Na_2AuB_6: the low-frequency contribution mainly originates from the pronounced softening along the M−Γ direction involving B/Au atom vibrations along the Au–B bond, while the mid-frequency contribution arises from the B_{2g} mode associated with the vibrations of B atoms along the Au−B bond axis (Fig. 3g, h). In contrast, in K_2AuB_6, λ arises from mid-frequency phonons, corresponding to vibrations of B atoms along the Au−B bond axis (Supplementary Fig. S16c, d). This distinction stems from stronger Au−B bonding in Na_2AuB_6, enabled by the smaller ionic radius of Na (Fig. 3i). Therefore, the higher T_c of Na_2AuB_6 compared to K_2AuB_6 arises from the synergistic effects of an enhanced Fermi-level DOS and stronger Au–B bonding strength.

Conclusions

In summary, we have investigated the stabilization of Au−B bonds through the incorporation of electropositive elements and pressure tuning, which led to the discovery of metallic M_2AuB_6 compounds (where M = Na, K, Mg, Ca,

and Sr). These compounds feature distinctive bonding configurations, including Au−B σ-bonds stabilized by dsp^2 hybridization, which remain robust under ambient conditions. Our findings underscore the crucial role of charge transfer and orbital hybridization in stabilizing these structures, contributing to their enhanced mechanical strength and thermal stability. Furthermore, we disclose superconductivity in K_2AuB_6 and Na_2AuB_6, with T_cs of 7.0 K and 10.2 K, respectively. The increased electron-phonon coupling, particularly from low-frequency phonons associated with Au−B bond vibrations, is identified as a key factor driving superconductivity in these materials. This discovery not only advances our understanding of Au-B chemistry but also opens up new avenues for unconventional bonding strategies in material design, with potential applications in creating functional materials with unique properties.

Methods

Structure searches of $Ca_xAu_yB_z$ ($x = 1-4$, $y = 1-2$, $z = 1-8$) at 50 GPa were performed using the Crystal structure AnaLYsis Particle Swarm Optimization (CALYPSO) code[91–93]. Structural optimization and electronic property calculations were carried out using density functional theory (DFT) as implemented in the Vienna Ab initio Simulation Package (VASP)[94]. The Perdew–Burke–Ernzerhof (PBE) generalized gradient approximation (GGA)[95] was employed for the exchange–correlation functional. The projector−augmented wave (PAW) method[96] was used, with valence electrons specified as $3s^23p^64s^2$ for Ca, $5d^{10}6s^1$ for Au, and $2s^22p^1$ for B. A cutoff energy of 550 eV was adopted, and the Monkhorst–Pack scheme[97] with a dense k-point grid spacing of $2\pi \times 0.03$ Å^{-1} was used to ensure excellent convergence of the enthalpy. Phonon calculations were carried out using the finite displacement method[98], as implemented in the PHONOPY code[99]. Ab initio MD simulations in the canonical ensemble (NVT) employed the Nose–Hoover thermostat[100], using a $2 \times 2 \times 2$ supercell with a time step of 1 fs over a total duration of 20 ps. The chemical bonding analysis was analyzed using the solid state adaptive natural density partitioning (SSAdNDP) method[79] at the 6–31 G*/ANO-R1 level of theory. The crystal orbital Hamilton population (COHP)[84] calculations were performed using the LOBSTER software package. Electron−phonon coupling calculations for superconductivity were performed with the QUANTUM−ESPRESSO package[101], employing a kinetic energy cutoff of 90 Ry. Further computational details are provided in Supplementary Methods.

Data availability

The data that support the findings of this study are available from the corresponding author upon reasonable request.

References

1. Mao, W. L. et al. Bonding changes in compressed superhard graphite. *Science* **302**, 425–427 (2003).
2. Goesten, M. G. Be−Be π-bonding and predicted superconductivity in MB_2 (M = Zr, Hf). *Angew. Chem. Int. Ed.* **61**, e202114303 (2022).
3. Lavroff, R. H., Munarriz, J., Dickerson, C. E., Munoz, F. & Alexandrova, A. N. Chemical bonding dictates drastic critical temperature difference in two seemingly identical superconductors. *Proc. Natl. Acad. Sci. USA* **121**, e2316101121 (2024).
4. Belli, F., Novoa, T., Contreras-García, J. & Errea, I. Strong correlation between electronic bonding network and critical temperature in hydrogen-based superconductors. *Nat. Commun.* **12**, 5381 (2021).
5. Wang, X. et al. The microscopic diamond anvil cell: stabilization of superhard, superconducting carbon allotropes at ambient pressure. *Angew. Chem. Int. Ed.* **61**, e202205129 (2022).
6. Green, J. C., Green, M. L. H. & Parkin, G. The occurrence and representation of three-centre two-electron bonds in covalent inorganic compounds. *Chem. Commun.* **48**, 11481–11503 (2012).

7. Eberhardt, W. H., Crawford, B. Jr & Lipscomb, W. N. The valence structure of the boron hydrides. *J. Chem. Phys.* **22**, 989–1001 (1954).

8. Miao, M. S. Caesium in high oxidation states and as a *p*-block element. *Nat. Chem.* **5**, 846–852 (2013).

9. Dong, X. et al. A stable compound of helium and sodium at high pressure. *Nat. Chem.* **9**, 440–445 (2017).

10. Lin, J. et al. Exploring the limits of transition-metal fuorination at high pressures. *Angew. Chem. Int. Ed.* **59**, 9155–9162 (2020).

11. Zhang, X. et al. Au with sp^3 Hybridization in Li_5AuP_2. *J. Phys. Chem. Lett.* **13**, 236–242 (2022).

12. Sommer, A. Alloys of gold with alkali metals. *Nature* **152**, 215–215 (1943).

13. Drozdov, A. P. et al. Superconductivity at 250 K in lanthanum hydride under high pressures. *Nature* **569**, 528–531 (2019).

14. Li, Z. et al. Superconductivity above 200 K discovered in superhydrides of calcium. *Nat. Commun.* **13**, 2863 (2022).

15. Ma, L. et al. High-temperature superconducting phase in clathrate calcium hydride CaH_6 up to 215 K at a pressure of 172 GPa. *Phys. Rev. Lett.* **128**, 167001 (2022).

16. Li, Q. et al. Superhard monoclinic polymorph of carbon. *Phys. Rev. Lett.* **102**, 175506 (2009).

17. Zhao, Z. et al. Novel superhard carbon: C-centered orthorhombic C_8. *Phys. Rev. Lett.* **107**, 215502 (2011).

18. Zhang, M. et al. Superhard BC_3 in cubic diamond structure. *Phys. Rev. Lett.* **114**, 015502 (2015).

19. Gimeno, M. C. & Laguna, A. Some recent highlights in gold chemistry. *Gold. Bull.* **36**, 83–92 (2003).

20. Jiang, D. -e & Walter, M. Au_{40}: a large tetrahedral magic cluster. *Phys. Rev. B* **84**, 193402 (2011).

21. Pyykkö, P. Theoretical chemistry of gold. *Angew. Chem. Int. Ed.* **43**, 4412–4456 (2004).

22. Pyykkö, P. Relativistic effects in chemistry: more common than you thought. *Annu. Rev. Phys. Chem.* **63**, 45–64 (2012).

23. Hutchings, G. J., Brust, M. & Schmidbaur, H. Gold—an introductory perspective. *Chem. Soc. Rev.* **37**, 1759–1765 (2008).

24. Faltens, M. O. & Shirley, D. A. Mössbauer spectroscopy of gold compounds. *J. Chem. Phys.* **53**, 4249–4264 (1970).

25. Lin, J., Zhang, S., Guan, W., Yang, G. & Ma, Y. Gold with +4 and +6 oxidation states in AuF_4 and AuF_6. *J. Am. Chem. Soc.* **140**, 9545–9550 (2018).

26. Yang, G., Wang, Y., Peng, F., Bergara, A. & Ma, Y. Gold as a 6*p*-element in dense lithium aurides. *J. Am. Chem. Soc.* **138**, 4046–4052 (2016).

27. Du, X., Lou, H., Wang, J. & Yang, G. Pressure-induced Na–Au compounds with novel structural units and unique charge transfer. *Phys. Chem. Chem. Phys.* **23**, 6455–6461 (2021).

28. Schmidbaur, H. & Schier, A. A briefing on aurophilicity. *Chem. Soc. Rev.* **37**, 1931–1951 (2008).

29. Schmidbaur, H. & Schier, A. Aurophilic interactions as a subject of current research: an up-date. *Chem. Soc. Rev.* **41**, 370–412 (2012).

30. Hashmi, A. S. K. & Hutchings, G. J. Gold catalysis. *Angew. Chem. Int. Ed.* **45**, 7896–7936 (2006).

31. Wittstock, A. & Bäumer, M. Catalysis by unsupported skeletal gold catalysts. *Acc. Chem. Res.* **47**, 731–739 (2014).

32. Sanchis-Gual, R., Coronado-Puchau, M., Mallah, T. & Coronado, E. Hybrid nanostructures based on gold nanoparticles and functional coordination polymers: chemistry, physics and applications in biomedicine, catalysis and magnetism. *Coord. Chem. Rev.* **480**, 215025 (2023).

33. Zhang, Y. et al. Site-recognition-induced structural and photoluminescent evolution of the gold–pincer nanocluster. *J. Am. Chem. Soc.* **146**, 9631–9639 (2024).

34. Albert, B. & Hillebrecht, H. Boron: elementary challenge for experimenters and theoreticians. *Angew. Chem. Int. Ed.* **48**, 8640–8668 (2009).

35. Akopov, G., Yeung, M. T. & Kaner, R. B. Rediscovering the crystal chemistry of borides. *Adv. Mater.* **29**, 1604506 (2017).

36. Chen, T.-T. et al. Spherical trihedral metallo-borospherenes. *Nat. Commun.* **11**, 2766 (2020).

37. Jian, T. et al. Probing the structures and bonding of size-selected boron and doped-boron clusters. *Chem. Soc. Rev.* **48**, 3550–3591 (2019).

38. Oganov, A. R. et al. Ionic high-pressure form of elemental boron. *Nature* **457**, 863–867 (2009).

39. Chung, H.-Y. et al. Synthesis of ultra-incompressible superhard rhenium diboride at ambient pressure. *Science* **316**, 436–439 (2007).

40. Gu, Q., Krauss, G. & Steurer, W. Transition metal borides: superhard versus ultra-incompressible. *Adv. Mater.* **20**, 3620–3626 (2008).

41. Akopov, G. et al. Synthesis and characterization of single-phase metal dodecaboride solid solutions: $Zr_{1-x}Y_xB_{12}$ and $Zr_{1-x}U_xB_{12}$. *J. Am. Chem. Soc.* **141**, 9047–9062 (2019).

42. Huang, H. et al. Deep-ultraviolet nonlinear optical materials: $Na_2Be_4B_4O_{11}$ and $LiNa_5Be_{12}B_{12}O_{33}$. *J. Am. Chem. Soc.* **135**, 18319–18322 (2013).

43. Ma, C. et al. Strong chiroptical nonlinearity in coherently stacked boron nitride nanotubes. *Nat. Nanotechnol.* **19**, 1299–1305 (2024).

44. Wang, Y. et al. Two-dimensional molybdenum boride (MBene) $Mo_{4/3}B_2T_x$ with broadband and termination-dependent ultrafast nonlinear optical response. *J. Phys. Chem. Lett.* **15**, 3461–3469 (2024).

45. Zhao, B. et al. Fabrication of alkali metal boride: honeycomb-like structured NaB_4 with high hardness and excellent electrical conductivity. *Adv. Funct. Mater.* **32**, 2110872 (2022).

46. Ma, T. et al. Ultrastrong boron frameworks in ZrB_{12}: a highway for electron conducting. *Adv. Mater.* **29**, 1604003 (2017).

47. Huang, M.-X. et al. Hard copper boride with exceptional conductivity. *Phys. Rev. Lett.* **133**, 136301 (2024).

48. Gou, H. et al. Discovery of a superhard iron tetraboride superconductor. *Phys. Rev. Lett.* **111**, 157002 (2013).

49. Tang, H. et al. Boron-rich molybdenum boride with unusual short-range vacancy ordering, anisotropic hardness, and superconductivity. *Chem. Mater.* **32**, 459–467 (2019).

50. Nagamatsu, J., Nakagawa, N., Muranaka, T., Zenitani, Y. & Akimitsu, J. Superconductivity at 39 K in magnesium diboride. *Nature* **410**, 63–64 (2001).

51. Souma, S. et al. The origin of multiple superconducting gaps in MgB_2. *Nature* **423**, 65–67 (2003).

52. Braunschweig, H. et al. A trimetallic gold boride complex with a fluxional gold–boron bond. *Angew. Chem. Int. Ed.* **48**, 9735–9738 (2009).

53. Zhai, H.-J., Miao, C.-Q., Li, S.-D. & Wang, L.-S. On the analogy of B−BO and B−Au chemical bonding in $B_{11}O^-$ and $B_{10}Au^-$ clusters. *J. Phys. Chem. A* **114**, 12155–12161 (2010).

54. Chen, Q., Zhai, H.-J., Li, S.-D. & Wang, L.-S. On the structures and bonding in boron-gold alloy clusters: $B_6Au_n^-$ and B_6Au_n ($n = 1−3$). *J. Chem. Phys.* **138**, 084306 (2013).

55. Obrowski, W. Die Struktur der Diboride von Gold und Silber. *Naturwissenschaften* **48**, 428–428 (1961).

56. Kortus, J., Mazin, I. I., Belashchenko, K. D., Antropov, V. P. & Boyer, L. L. Superconductivity of metallic boron in MgB_2. *Phys. Rev. Lett.* **86**, 4656–4659 (2001).

57. Yang, F., Han, R.-S., Tong, N.-H. & Guo, W. Electronic structural properties and superconductivity of diborides in the MgB_2 structure. *Chin. Phys. Lett.* **19**, 1336 (2002).

58. Mann, J. B., Meek, T. L., Knight, E. T., Capitani, J. F. & Allen, L. C. Configuration energies of the *d*-block elements. *J. Am. Chem. Soc.* **122**, 5132–5137 (2000).

59. Mann, J. B., Meek, T. L. & Allen, L. C. Configuration energies of the main group elements. *J. Am. Chem. Soc.* **122**, 2780–2783 (2000).

60. Rahm, M., Hoffmann, R. & Ashcroft, N. W. Ternary gold hydrides: routes to stable and potentially superconducting compounds. *J. Am. Chem. Soc.* **139**, 8740–8751 (2017).

61. Dubois, J.-M., Belin-Ferré, E. & Tsai, A. P. Quasicrystals and Complex Metallic Alloys. In *Kirk-Othmer Encyclopedia of Chemical Technology* (Wiley, 2016).

62. Burkhardt, F. et al. A new complex ternary phase in the Al-Cr-Sc push-pull alloy. *J. Alloy. Compd.* **768**, 230–239 (2018).

63. Kelhar, L. et al. The role of Fe and Cu additions on the structural, thermal and magnetic properties of amorphous Al-Ce-Fe-Cu alloys. *J. Non Cryst. Solids* **483**, 70–78 (2018).

64. Boulet, P. et al. Crystalline and electronic structures of the $Al_{1+x}V_2Sn_{2-x}$ ($x = 0.19$) intermetallic compound. *Inorg. Chem.* **59**, 360–366 (2020).

65. Zhang, L., Wang, Y., Lv, J. & Ma, Y. Materials discovery at high pressures. *Nat. Rev. Mater.* **2**, 17005 (2017).

66. Miao, M., Sun, Y., Zurek, E. & Lin, H. Chemistry under high pressure. *Nat. Rev. Chem.* **4**, 508–527 (2020).

67. Miao, M.-S. & Hoffmann, R. High pressure electrides: a predictive chemical and physical theory. *Acc. Chem. Res.* **47**, 1311–1317 (2014).

68. Oganov, A. R., Pickard, C. J., Zhu, Q. & Needs, R. J. Structure prediction drives materials discovery. *Nat. Rev. Mater.* **4**, 331–348 (2019).

69. Hilleke, K. P. & Zurek, E. 3.13-Crystal Chemistry at High Pressure. In *Comprehensive Inorganic Chemistry III* 3rd edn (eds Reedijk J., Poeppelmeier K. R.) (Elsevier, 2023).

70. Han, S. et al. Pressure-driven charge transfer and tunable superconductivity in intermetallic Li–Mg electrides. *Superconductivity* **15**, 100187 (2025).

71. Vlasse, M., Slack, G. A., Garbauskas, M., Kasper, J. S. & Viala, J. C. The crystal structure of SiB_6. *J. Solid. State Chem.* **63**, 31–45 (1986).

72. Yuan, Z., Xiong, M. & Yu, D. A novel metallic silicon hexaboride, *Cmca*-B_6Si. *Phys. Lett. A* **384**, 126075 (2020).

73. Wang, J.-T. et al. Body-centered orthorhombic C_{16}: a novel topological node-line semimetal. *Phys. Rev. Lett.* **116**, 195501 (2016).

74. Kroto, H. W., Heath, J. R., O'Brien, S. C., Curl, R. F. & Smalley, R. E. C_{60}: Buckminsterfullerene. *Nature* **318**, 162–163 (1985).

75. Li, D., Xu, Y.-N. & Ching, W. Y. Electronic structures, total energies, and optical properties of *a*-rhombohedral B_{12} and *a*-tetragonal B_{50} crystals. *Phys. Rev. B* **45**, 5895–5905 (1992).

76. Cordier, G., Dietrich, C. & Friedrich, T. Crystal structures of europium digold pentagallide, $EuAu_2Ga_5$ and strontium digold pentagallide, $SrAu_2Ga_5$. *Z. Anorg. Allg. Chem.* **211**, 627–628 (1996).

77. Offermanns, J., Ruschewitz, U. & Kneip, C. Syntheses and crystal structures of novel ternary alkali metal gold acetylides M^IAuC_2 ($MI = Li$, Na, K, Rb, Cs). *Z. Anorg. Allg. Chem.* **626**, 649–654 (2000).

78. Sun, Y. & Miao, M. Chemical templates that assemble the metal superhydrides. *Chem* **9**, 443–459 (2023).

79. Zubarev, D. Y. & Boldyrev, A. I. Developing paradigms of chemical bonding: adaptive natural density partitioning. *Phys. Chem. Chem. Phys.* **10**, 5207–5217 (2008).

80. Corbett, J. D. Exploratory synthesis: the fascinating and diverse chemistry of polar intermetallic phases. *Inorg. Chem.* **49**, 13–28 (2010).

81. Lin, Q. & Miller, G. J. Electron-poor polar intermetallics: complex structures, novel clusters, and intriguing bonding with pronounced electron delocalization. *Acc. Chem. Res.* **51**, 49–58 (2018).

82. Maintz, S., Deringer, V. L., Tchougréeff, A. L. & Dronskowski, R. LOBSTER: a tool to extract chemical bonding from plane-wave based DFT. *J. Comput. Chem.* **37**, 1030–1035 (2016).

83. Müller, P. C., Reitz, L. S., Hemker, D. & Dronskowski, R. Orbital-based bonding analysis in solids. *Chem. Sci.* **16**, 12212–12226 (2025).

84. Dronskowski, R. & Bloechl, P. E. Crystal orbital Hamilton populations (COHP): energy-resolved visualization of chemical bonding in solids based on density-functional calculations. *J. Phys. Chem.* **97**, 8617–8624 (1993).

85. Simon, A. Superconductivity and chemistry. *Angew. Chem. Int. Ed.* **36**, 1788–1806 (1997).

86. Pereira, Z. S., Faccin, G. M. & da Silva, E. Z. Predicted superconductivity in the electride Li_5C. *J. Phys. Chem. C* **125**, 8899–8906 (2021).

87. Allen, P. B. & Dynes, R. C. Transition temperature of strong-coupled superconductors reanalyzed. *Phys. Rev. B* **12**, 905–922 (1975).

88. Kitagawa, S. et al. Pressure-induced superconductivity in mineral calaverite $AuTe_2$. *J. Phys. Soc. Jpn.* **82**, 113704 (2013).

89. Kudo, K. et al. Superconductivity induced by breaking Te_2 dimers of $AuTe_2$. *J. Phys. Soc. Jpn.* **82**, 063704 (2013).

90. Amiel, Y. et al. Silvanite $AuAgTe_4$: a rare case of gold superconducting material. *J. Mater. Chem. C* **11**, 10016–10024 (2023).

91. Wang, Y., Lv, J., Zhu, L. & Ma, Y. Crystal structure prediction via particle-swarm optimization. *Phys. Rev. B* **82**, 094116 (2010).

92. Wang, Y., Lv, J., Zhu, L. & Ma, Y. CALYPSO: a method for crystal structure prediction. *Comput. Phys. Commun.* **183**, 2063–2070 (2012).

93. Shao, X. et al. A symmetry-orientated divide-and-conquer method for crystal structure prediction. *J. Chem. Phys.* **156**, 014105 (2022).

94. Kresse, G. & Furthmüller, J. Efficiency of ab-initio total energy calculations for metals and semiconductors using a plane-wave basis set. *Comput. Mater. Sci.* **6**, 15–50 (1996).

95. Perdew, J. P., Burke, K. & Ernzerhof, M. Generalized gradient approximation made simple. *Phys. Rev. Lett.* **77**, 3865–3868 (1996).

96. Kresse, G. & Joubert, D. From ultrasoft pseudopotentials to the projector augmented-wave method. *Phys. Rev. B* **59**, 1758 (1999).

97. Monkhorst, H. J. & Pack, J. D. Special points for Brillouin-zone integrations. *Phys. Rev. B* **13**, 5188 (1976).

98. Parlinski, K., Li, Z. Q. & Kawazoe, Y. First-principles determination of the soft mode in cubic ZrO_2. *Phys. Rev. Lett.* **78**, 4063–4066 (1997).

99. Togo, A., Oba, F. & Tanaka, I. First-principles calculations of the ferroelastic transition between rutile-type and $CaCl_2$-type SiO_2 at high pressures. *Phys. Rev. B* **78**, 134106 (2008).

100. Martyna, G. J., Klein, M. L. & Tuckerman, M. Nosé–Hoover chains: the canonical ensemble via continuous dynamics. *J. Chem. Phys.* **97**, 2635–2643 (1992).

101. Giannozzi, P. et al. QUANTUM ESPRESSO: a modular and open-source software project for quantum simulations of materials. *J. Phys. Condens. Matter* **21**, 395502 (2009).

Acknowledgements

Author contributions

S.H. performed calculations, analyzed the data, and wrote the original draft; X.Z., S.W., and S.D. assisted the calculations, and participated in the data analysis; L.Z., E.Z., and G.Y. wrote and modified the manuscript; G.Y. conceived the initial idea and supervised the project.

Competing interests

The authors declare no competing interests.

Additional information